

## DEVELOPMENT

# Cilia function as calcium-mediated mechanosensors that instruct left-right asymmetry

Lydia Djenoune<sup>1†</sup>, Mohammed Mahamdeh<sup>1†</sup>, Thai V. Truong<sup>2</sup>, Christopher T. Nguyen<sup>1,3,4</sup>, Scott E. Fraser<sup>2</sup>, Martina Brueckner<sup>5</sup>, Jonathon Howard<sup>6</sup>, Shialou Yuan<sup>1\*</sup>

The breaking of bilateral symmetry in most vertebrates is critically dependent upon the motile cilia of the embryonic left-right organizer (LRO), which generate a directional fluid flow; however, it remains unclear how this flow is sensed. Here, we demonstrated that immotile LRO cilia are mechanosensors for shear force using a methodological pipeline that combines optical tweezers, light sheet microscopy, and deep learning to permit *in vivo* analyses in zebrafish. Mechanical manipulation of immotile LRO cilia activated intraciliary calcium transients that required the cation channel Polycystin-2. Furthermore, mechanical force applied to LRO cilia was sufficient to rescue and reverse cardiac situs in zebrafish that lack motile cilia. Thus, LRO cilia are mechanosensitive cellular levers that convert biomechanical forces into calcium signals to instruct left-right asymmetry.

In human, rodent, amphibian, and fish embryos, left-right (LR) asymmetry is determined at the left-right organizer (LRO) by cilia that produce and transduce directional flow of extracellular fluid into asymmetric Nodal signaling and organ laterality (1–13). However, the mechanism by which cilia sense LRO flow is unknown (14–17), resulting in two leading hypotheses: Cilia are chemosensors of morphogens carried by flow (2, 18) or mechanosensors of force exerted by flow

(1, 5, 19, 20). Previous work connects asymmetric calcium signals with LRO flow and LR development (1, 5, 20, 21). However, it has been impossible to determine whether ciliary mechanosensation or chemosensation mediates these asymmetric calcium signals due to inadequate techniques for delivery of mechanical force or chemical cues specifically to LRO cilia *in vivo* (14, 15).

We developed and deployed an *in vivo* method to apply precise, localized mechanical forces onto LRO cilia in zebrafish. Our optical toolbox couples optical tweezers, light sheet microscopy, and deep learning analyses to deflect cilia and measure intraciliary calcium signaling in the zebrafish LRO. Combining these tools with longitudinal assays, we revealed that the cilium is a calcium-mediated mechanosensor that is necessary, sufficient, and instructive for LR development.

## Cilia can be optically deflected

Prior studies of cilia mechanosensation applied laminar fluid flow across both the cilium

and apical plasma membrane, limiting identification of a cilia-specific mechanical signal (22–25). Further, laminar flow approaches may transport chemical cues in addition to mechanical stimulation. To deflect cilia in a specific and controllable manner *in vivo*, we devised a strategy that employs optical tweezers to apply local mechanical forces onto cilia. The ability of optical tweezers to use light to exert and measure mechanical forces onto structures ranging in size from microns to nanometers makes them ideally suited for single cells, proteins, and molecules (26–28). We employed optical tweezers to bend cilia by directly trapping them and applying force without the need for tethered beads or microscope stage movements (which may confound ciliary signaling). Our integration of optical tweezers and fluorescence microscopy in a custom-built instrument permitted simultaneous recording with cilia-targeted fluorescent calcium reporters. This enabled fully programmable, precise spatiotemporal control of ciliary bending in both zebrafish embryos and cultured cells, and exact recapitulation of *in vivo* physiological conditions.

We validated our cilia deflection approach on LLC-PK1 porcine renal epithelial cells, as they have long immotile cilia and are amenable to transfection (20). We trapped the distal tip of the cilium by focusing the laser onto cilia of wild-type (WT) LLC-PK1 cells, and mechanically bent the cilium by steering the trapping laser with piezoelectric-actuated mirrors (fig. S1, A and B, and movie S1). All deflection parameters (frequency, displacement, angularity, direction, and duration) were precisely and remotely controlled (fig. S1, C and F). To recapitulate physiological conditions in which primary cilia are subjected to and bent by pulsatile shear fluid flow, such as in the kidney ducts and vasculature (29, 30), our optical tweezers were programmed to apply oscillatory deflection patterns to cilia at defined bending frequencies. Transfection

<sup>1</sup>Cardiovascular Research Center, Cardiology Division, Department of Medicine, Massachusetts General Hospital and Harvard Medical School, Boston, MA 02129, USA.

<sup>2</sup>Translational Imaging Center, University of Southern California, Los Angeles, CA 90089, USA. <sup>3</sup>Cardiovascular Innovation Research Center, Heart, Vascular, and Thoracic Institute, Cleveland Clinic, Cleveland, OH 44195, USA.

<sup>4</sup>Division of Health Science Technology, Massachusetts Institute of Technology, Cambridge, MA 02139, USA.

<sup>5</sup>Departments of Pediatrics and Genetics, Yale University School of Medicine, New Haven, CT 06520, USA.

<sup>6</sup>Department of Molecular Biochemistry and Biophysics, Yale University School of Medicine, New Haven, CT 06520, USA.

\*Corresponding author. Email: shialou.yuan@mgh.harvard.edu

†These authors contributed equally to this work.

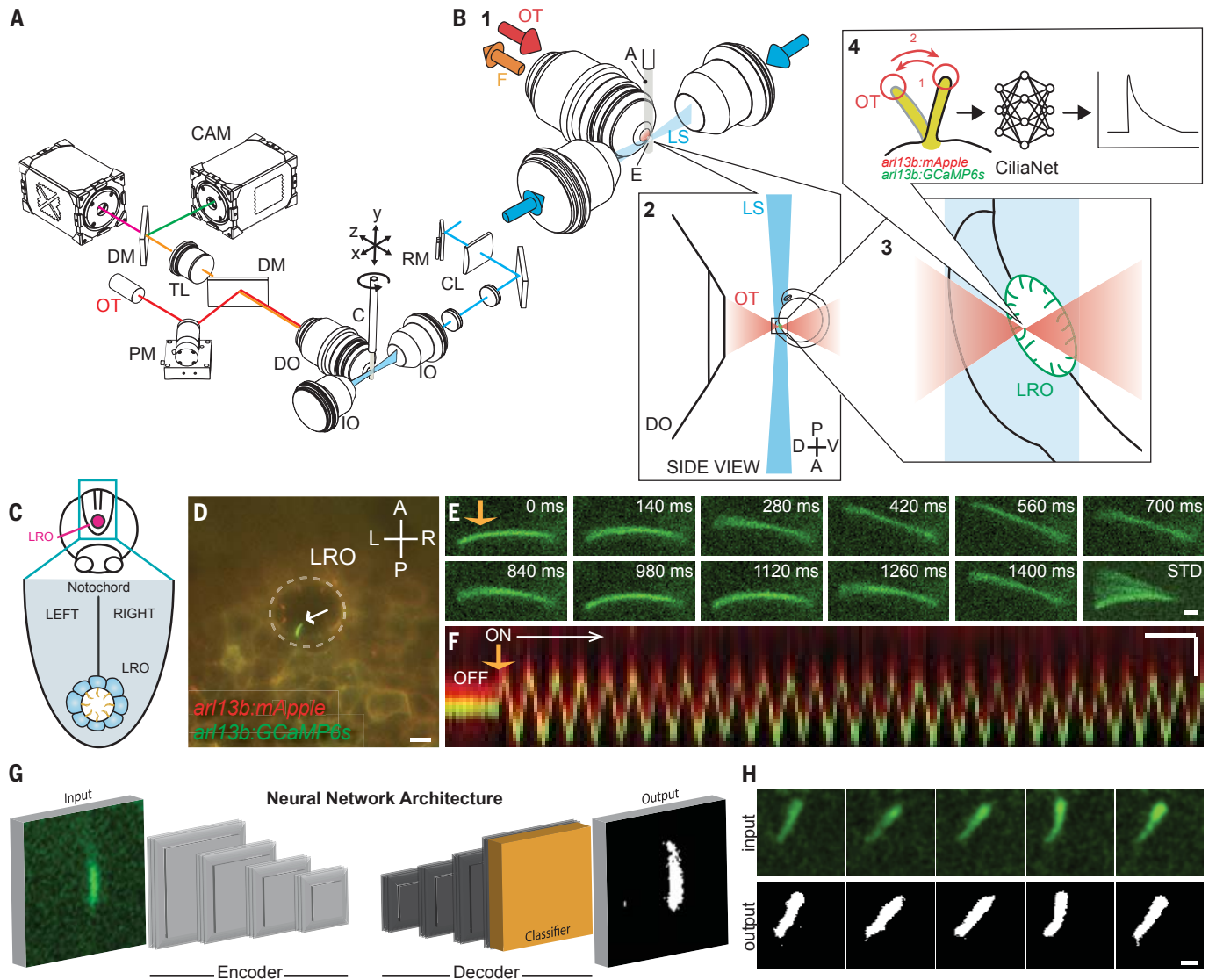


**Fig. 1. CiliaSPOT is a precise and tunable platform for cilia mechanosensing studies.** (A) Mechanical drawing of the CiliaSPOT microscope highlighting key components. For detailed description of the setup, see Materials and Methods and fig. S3. (B) Trapping and analyzing ciliary responses in the LRO of zebrafish embryos. (1) Close-up view showing the zebrafish embryo mounted in an agarose column extruded from a glass capillary. The cilia are fluorescently excited by the light sheet. (2) Side view of the optical trap and the LRO of a zebrafish embryo mounted in agarose. (3) Trapping of a single cilium in the LRO (green). (4) The trapped cilium is bent in an oscillatory fashion while being imaged. Images are then processed and analyzed by the CiliaNet machine learning algorithm to track and measure cilia responses to bending. A, agarose column; C, capillary; CL, cylindrical lens; CAM, camera; DM, dichroic mirror; DO, detection objective; E, embryo; F, fluorescence signal; IO, illumination objective; LS, light sheet; OT, optical trapping laser; PM, piezo mirror; RM, resonant mirror; TL, tube lens. (C) Illustration representing the LRO in the zebrafish embryo. (D) Representative image of an embryo expressing the ratiometric ciliary calcium reporter (*arl13b:mApple;arl13b:GCaMP6s*) with an intraciliary calcium oscillation (ICO, white arrow) within the LRO (dashed line). Scale: 10  $\mu\text{m}$ . A, anterior; P, posterior; L, left; R, right; LRO, left-right organizer. (E) Representative montage of a fluorescent LRO cilium being bent by the optical trap (orange arrow) in vivo. Numbers indicate time after start of the bend. STD represents the standard deviation Z-projection of the montage. Scale: 2  $\mu\text{m}$ . (F) Representative kymograph of an LRO cilium being bent by the optical trap (orange arrow). Note here that the GCaMP6s and mApple signals are kept slightly shifted for illustration purposes (see Materials and Methods and fig. S4). Scales: vertical: 2  $\mu\text{m}$ ; horizontal: 2 s. (G) Illustration of CiliaNet segmentation workflow. (H) Representative montage of sequential images of an LRO cilium dynamically trapped and moved by the optical tweezers (input) annotated by CiliaNet (output). Scale: 2  $\mu\text{m}$ .

of LLC-PK1 cells with the fluorescent cilia marker transgene *arl13b:EGFP* (20) permitted us to validate simultaneous optical oscillatory bending and fluorescence microscopy (fig. S1, D to F, and movie S2).

The in vivo dynamics of immotile cilia in the zebrafish LRO were investigated with high-

resolution differential interference contrast imaging (fig. S2 and movie S3). Measurements of ciliary angle and frequency displacement revealed that cilia on the left side of the LRO were subjected to greater angle displacements than cilia on the right side (fig. S2, B and C), consistent with the stronger flow on the left side

of the LRO (4, 7, 9, 10, 31). We also observed small and slow displacement frequencies of LRO cilia (fig. S2D), with no significant difference between the two sides (fig. S2E). Our computer-controlled tweezer motions of LRO cilia were guided by these parameters, mimicking their in vivo bending dynamics.

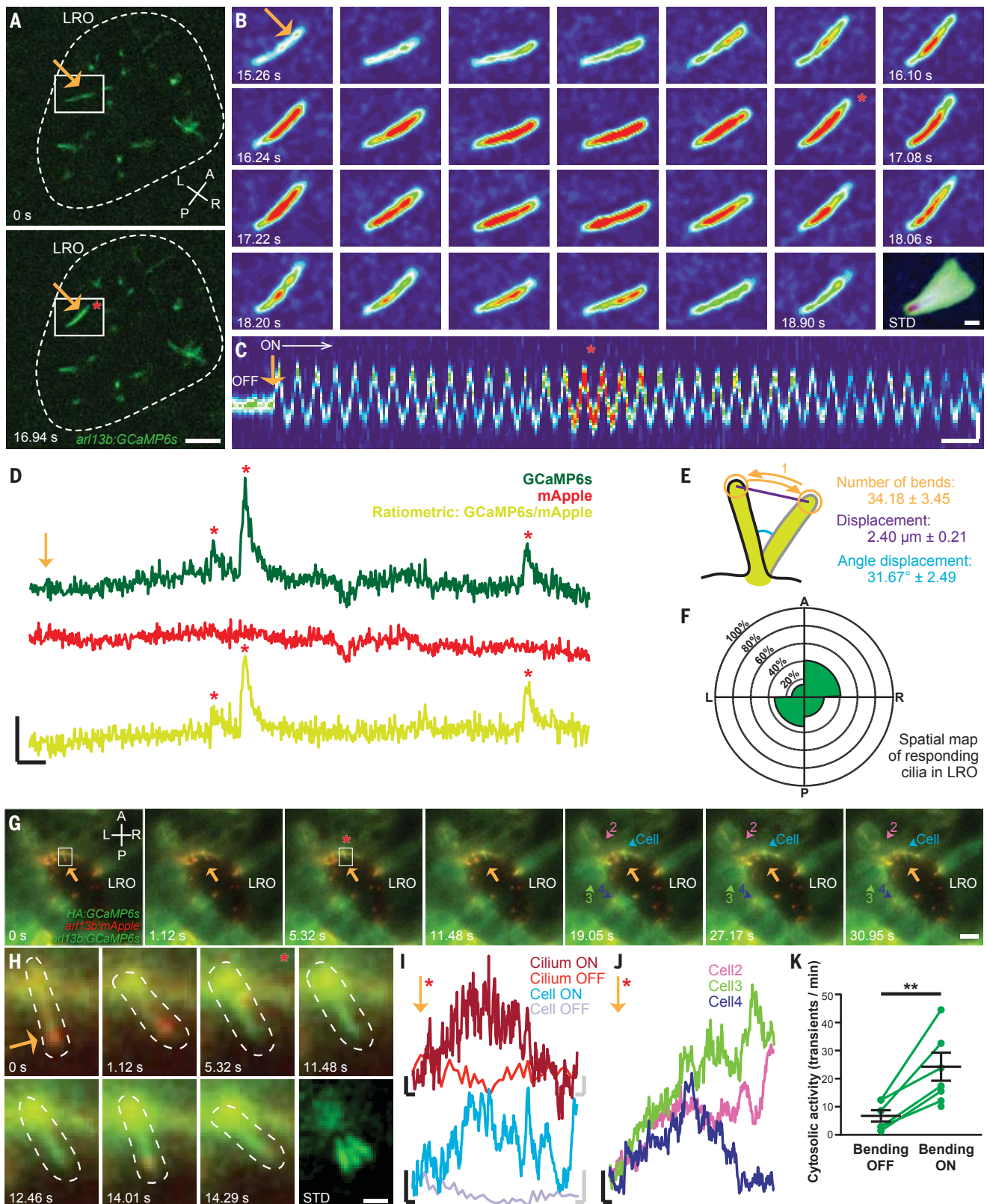


**Fig. 2. Oscillatory mechanical stimuli on LRO cilia activate intraciliary calcium transients.** (A) Representative images of the LRO of a *c21orf59* morphant zebrafish. Dashed line: LRO. Scale: 10  $\mu\text{m}$ . (B) Representative montage of the GCaMP6s-positive LRO cilium highlighted in (A). Scale: 2  $\mu\text{m}$ . (C) Kymograph of the cilium shown in (B) before ("OFF") and during optical bending ("ON",

white arrow, starting at orange arrow). Scales: vertical: 2  $\mu\text{m}$ ; horizontal: 2 s. (D) Intraciliary intensity over time plots of a single LRO cilium exhibiting intraciliary calcium oscillations of different amplitudes in response to optical bending. Scales: vertical: 50%  $\Delta\text{F}/\text{F}$ ; horizontal: 5 s. (E) Optical bending characteristics associated with responding LRO cilia. Mean  $\pm$  S.E.M.,  $n = 23$  responses analyzed. (F) Spatial

**EMBARGOED UNTIL 2PM U.S. EASTERN TIME ON THE THURSDAY BEFORE THIS DATE:**

mapping of ciliary responses in the *c21orf59* embryos. Mean percentage of ciliary responses to optical bending in each region of the LRO ( $n = 88$  cilia from 12 embryos). No statistical differences were observed between LRO regions (Fisher's exact tests with Bonferroni correction, all  $P > 0.05$ ). (G) Representative montage of cytosolic calcium responses (colored arrowheads) following the intraciliary calcium response of a LRO cilium (white box) to oscillatory optical bending (orange arrow). Scale: 10  $\mu\text{m}$ . (H) Representative montage of the cilium (dashed line) highlighted in (G). Scale: 2  $\mu\text{m}$ . (I) GCaMP6s intensity over time plots of the cilium bent in (G) and (H) and in the connected cell (G), before (OFF) and after (ON) the start of the optical mechanical

stimulation. Black scales for ON traces: vertical: 20%  $\Delta\text{F}/\text{F}$ ; horizontal: 2 s. Gray scales for OFF traces: vertical: 20%  $\Delta\text{F}/\text{F}$ ; horizontal: 0.3 s. (J) GCaMP6s intensity over time plots of the responding cells highlighted in (G). (K) Mean frequency of cytosolic activity (number of calcium transients per minute) at rest before bending (bending OFF) and during bending by the optical tweezers (bending ON) in *c21orf59* embryos ( $n = 6$  morphants).  $^{***}P < 0.01$  ( $P$ -value = 0.0044), paired two-tailed  $t$ -test. A, anterior; P, posterior; L, left; R, right; LRO, left-right organizer. Orange arrows: optical mechanical stimulation; red asterisks: start of the intraciliary response; numbers: time after start of the bend; STD: standard deviation Z-projection of montage.

To facilitate simultaneous live imaging of intraciliary calcium signaling and cilia deflection studies during LR development in zebrafish, we constructed a custom ciliary selective plane illumination microscope with optical tweezers ("CiliaSPOT", Fig. 1, A and B, and fig. S3). Selective plane illumination microscopy (light sheet microscopy) provides fast and gentle imaging of dynamic *in vivo* processes such as calcium signaling as a result of its rapid optical sectioning capabilities and reduced photobleaching (32, 33).

The performance of CiliaSPOT was validated on immotile cilia in the LRO of 1-4 somite stage (ss) zebrafish embryos expressing a cilia-targeted ratiometric fluorescence calcium indicator system (*arll3b:GCaMP6s;arll3b:mApple*), which we previously used to discover intraciliary calcium transients in the LRO (20). CiliaSPOT efficiently trapped the fluorescent cilia in the LRO with only 100 mW of laser power and was able to deflect immotile cilia in an oscillatory fashion mimicking their normal motions *in vivo* (Fig. 1, C to F, fig. S4, and movie S4). The amount of force applied to LRO cilia by CiliaSPOT was estimated to be 0.6 pN (fig. S5), in line with the estimated *in vivo* flow forces on LRO cilia (0.1 pN, Materials and Methods) and previous *in vitro* studies (34, 35).

To analyze the fluorescent imaging data, we created the ciliary neural network ("CiliaNet") for the automated tracking of moving cilia and extraction of fluorescence signal changes (Fig. 1, G and H, fig. S6, and movie S5). CiliaNet permitted rapid analysis of our high-speed (7 Hz), two-channel recordings of ciliary calcium dynamics, even in large recordings of several thousands of frames, streamlining quantification of ciliary calcium responses to optical bending. We validated CiliaNet accuracy on CiliaSPOT recordings by comparing manual- and machine-analyzed datasets: CiliaNet was eight times faster than manual analysis with similar fidelity (fig. S6, B to D). Together, CiliaSPOT and CiliaNet provide a powerful platform for experimentally testing and analyzing ciliary mechanosensation and calcium signaling.

### Mechanical stimulation of LRO cilia activates intraciliary calcium transients

Directional fluid flow in the LRO (described as leftward-biased in mice and counterclockwise

in zebrafish), driven by motile cilia, is necessary for LR development (3-5, 7-10, 12, 13). CiliaSPOT allowed us to determine the mechanistic link between this flow and the intraciliary calcium oscillations (ICOs) we and others have reported (20, 36). To determine whether the ICOs are mechanically generated in LRO cilia, CiliaSPOT was used to deflect immotile LRO cilia in zebrafish without endogenous fluid flow. Knocking down *c21orf59* results in an absence of LRO flow, deficient intraciliary calcium signaling, and complete randomization of cardiac LR asymmetry (20, 37), providing an ideal test setting. Any detectable elevations in intraciliary calcium or the presence of ICOs in *c21orf59* knockdown embryos must be solely due to our CiliaSPOT manipulation.

Intraciliary calcium transients were observed in immotile LRO cilia of *c21orf59* knockdown embryos trapped and bent in a controlled and oscillatory manner by CiliaSPOT (Fig. 2, A to D, Fig. 3, A to D, and movie S6). Prolonged mechanical oscillations, recapitulating the physiological ciliary behavior in the LRO of WT embryos with intact flow (20, 38), triggered repetitive intraciliary calcium transients that resembled previously described ICOs (20, 36) (Fig. 2D and movie S7). On average, intraciliary calcium transients occurred after  $34.2 \pm 3.5$  bends, with a displacement of  $2.4 \pm 0.2 \mu\text{m}$  and a deflection angle of  $31.7 \pm 2.5^\circ$  (Fig. 2E, mean  $\pm$  SEM, fig. S7). All cilia regardless of their location within the LRO could respond to CiliaSPOT deflection with intraciliary calcium transients (Fig. 2F), suggesting that the endogenous left-sided LRO ICOs are generated in response to force exerted by directional LRO flow. Calcium transients in response to CiliaSPOT bending of LRO cilia were not spatially autonomous, as the calcium transients often spread to the cell body, neighboring LRO cells, and mesodermal tissue around the LRO (Fig. 2, G to K, movie S8, and fig. S8).

CiliaSPOT oscillatory deflection of immotile LRO cilia of WT zebrafish (with intact endogenous counterclockwise fluid flow) activated intraciliary calcium transients (Fig. 3, F to J), regardless of the location of the manipulated cilia within the LRO (Fig. 3L). This not only reinforces our results from *c21orf59* knockdown embryos, but also suggests that immotile LRO cilia are capable of responding to mechanical stimuli, even while being

subjected to intrinsic counterclockwise flow. Collectively, our results demonstrate that the cilium is a bona fide mechanosensor that mediates calcium signaling in the LRO.

The observed increases in calcium activity were not due to photodamage or excessive heat from CiliaSPOT. No calcium transients beyond the baseline were observed in the LRO of *c21orf59* knockdown embryos from the application of the 100 mW optical tweezers without oscillatory motion, indicating that CiliaSPOT did not induce aberrant calcium activity in the LRO (fig. S9 and movie S9). Further, we calibrated and employed a heat-sensitive fluorescent dye, Rhodamine B, as an optical thermometer to quantify potential temperature elevations in our optical trapping plane (39). The very small temperature rise from the 100 mW optical tweezers laser was minimal ( $\sim 1^\circ\text{C}$ , fig. S10) and thus unlikely to cause heat-associated damage. A digital thermometer, used to measure global temperature changes inside the specimen chamber of CiliaSPOT, found an imperceptible elevation from the 100 mW optical tweezers, within the margin of error of the thermometer ( $\pm 0.1^\circ\text{C}$ , Materials and Methods). Combined, these data strongly suggest the absence of any CiliaSPOT laser-illumination-associated side effects that could have contributed to a false positive calcium signal.

### Ciliary mechanosensing at the LRO requires Polycystin-2

There are conflicting reports about whether the calcium-permeable cation channel Polycystin-2 (Pkd2) functions as a ciliary calcium channel and mechanosensor in a wide array of tissues (5, 14, 23, 24, 36, 40-42). Pkd2 localizes to all LRO cilia and is critical for left-sided ICOs in the LRO (20, 36) and normal LR patterning (1, 5, 43-45). In cultured ciliated renal cells, Pkd2 is proposed to be mechanosensitive for renal fluid flow, as application of artificial laminar fluid flow results in cytosolic calcium transients that require both the cilium and Pkd2 (22, 23). Such studies seem consistent with Pkd2 functioning as a molecular mechanosensor on cilia, regulating intraciliary calcium in response to mechanical forces exerted by flow.

To resolve the function of Pkd2 in the LRO, we utilized CiliaSPOT to mechanically bend

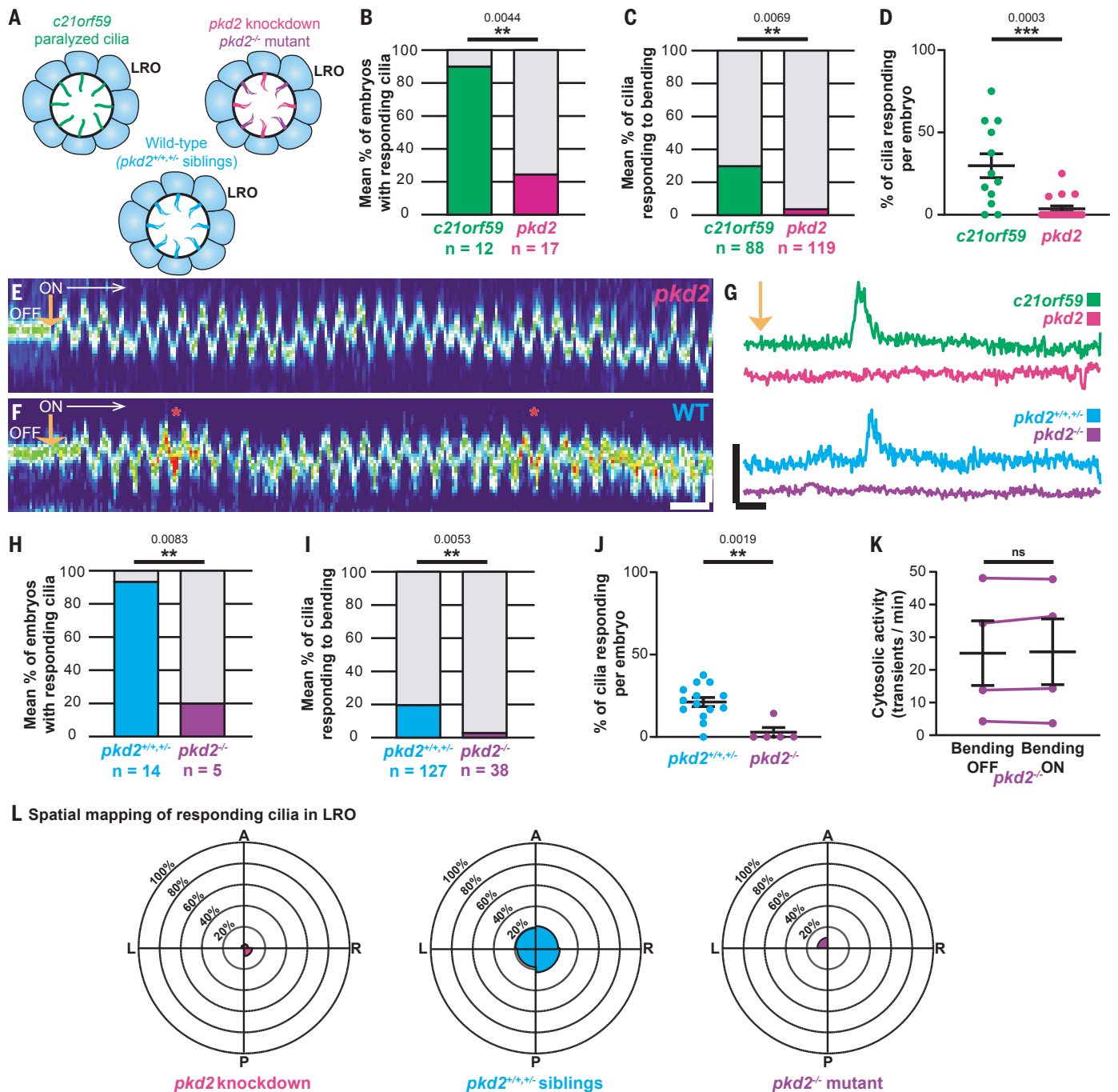


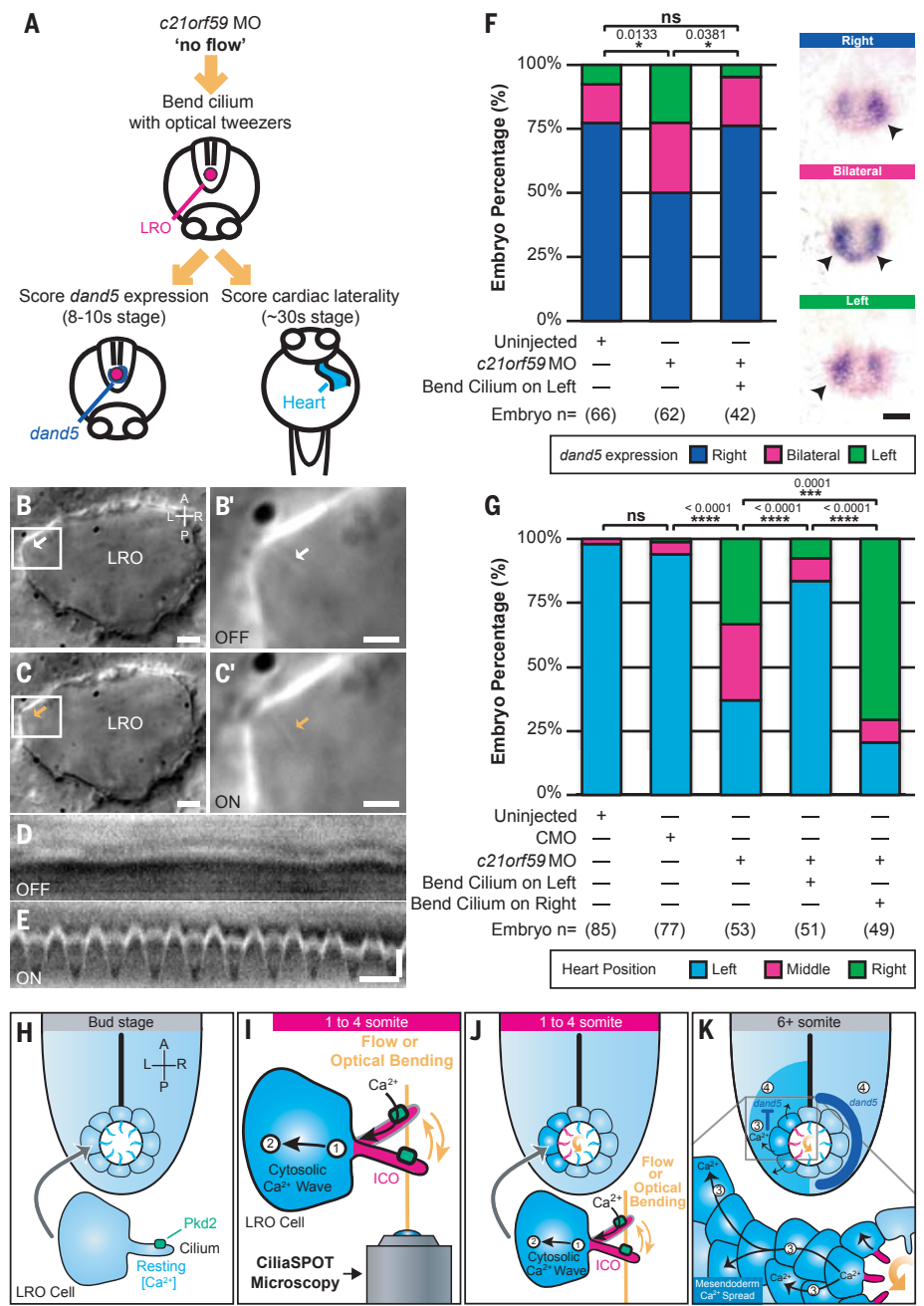
**Fig. 3. Ciliary mechanosensation requires Polycystin-2.** (A) Illustrations of the different models used in this study. (B to D) Percentage of embryos (B), cilia (C), and cilia per embryo (D) responding to optical bending in *c21orf59* (green, 88 cilia from 12 embryos) and *pkd2* morphants (magenta, 119 cilia from 17 embryos). Data shown are pooled from four independent experiments. Statistical comparison was analyzed by unpaired two-tailed *t*-tests; \*\**P* < 0.01 and \*\*\**P* < 0.001. (E and F) Representative kymographs of a LRO cilium from a *pkd2* morphant (E) and a WT (F) embryo showing their oscillatory motions and calcium activity in response to the optical bending (ON, white arrow, starting at orange arrow). Scales: vertical: 2  $\mu$ m; horizontal: 2 s. (G) Representative GCaMP6s intraciliary intensity over time plots of a single LRO cilium in response to optical bending in *c21orf59* (green) and *pkd2* (magenta) morphants, and in a *pkd2* mutant (purple) and WT sibling (blue). Scales: vertical: 100%  $\Delta$ F/F; horizontal: 5 s. (H to J) Percentage of embryos (H), cilia (I), and cilia per embryo

(J) responding to optical bending in WT siblings (total of 127 cilia from 14 embryos) and *pkd2* homozygous mutants (total of 38 cilia from 5 embryos). Data shown are pooled from five independent experiments. Statistical comparison was analyzed by unpaired two-tailed *t*-tests; \*\**P* < 0.01. (K) Mean frequency of cytosolic activity (number of calcium transients per minute) at rest before bending (bending OFF) compared with when LRO cilia are being bent by the optical tweezers (bending ON) in *pkd2* mutants. *n* = 4 mutants. ns, not significant, paired two-tailed *t*-test. (L) Spatial mapping of ciliary responses to optical bending in the *pkd2* knockdown (magenta), *pkd2* homozygous mutant (purple) and WT sibling (*pkd2*<sup>+/+/-</sup>, blue) zebrafish LROs. The rose diagrams represent the mean percentage of ciliary responses to optical bending in each region of the LRO. (*pkd2* knockdown = 119 cilia from 17 embryos; *pkd2* homozygous mutants = 38 cilia from 5 embryos; WT siblings *pkd2*<sup>+/+/-</sup> = 127 cilia from 14 embryos). A, anterior; P, posterior; L, left; R, right.

EMBARGOED UNTIL 2PM U.S. EASTERN TIME ON THE THURSDAY BEFORE THIS DATE:

**Fig. 4. Ciliary mechanosensation is determinative for LR asymmetry.**

**(A)** Schematic depicting the approach followed to assess *dand5* expression and cardiac laterality in *c21orf59* morphants (MO) after oscillatory optical bending of one LRO cilium. **(B to C')** Representative images of LRO cilia (arrows) from *c21orf59* embryos in the absence [(B) white arrow, OFF] or presence of optical tweezers [(C) orange arrow, ON]. [(B') and (C')] Cilium highlighted in white box in [(B) and (C)]. Scales: [(B) and (C)]: 5  $\mu$ m; [(B') and (C')]: 2  $\mu$ m. **(D and E)** Representative kymographs of LRO cilia from *c21orf59* embryos in the absence [(D) OFF] or presence of oscillatory optical tweezers [(E) ON]. Scales: vertical: 1  $\mu$ m; horizontal: 1 s. **(F)** Graph with illustrative pictures, representing percentage of uninjected and *c21orf59* morphants displaying normal right-sided (dark blue) and abnormal left-sided (green) or bilateral (magenta) *dand5* expression. *n* = total number of embryos analyzed. Statistical comparison was analyzed by a Pearson's chi-square test (Bonferroni corrected); \**P* < 0.05 and ns: *P*  $\geq$  0.05. Scale: 50  $\mu$ m. **(G)** Graph represents percentage of uninjected, control morpholino-injected (CMO) and *c21orf59* morphants displaying normal left-sided (light blue) and abnormal right-sided (green) or middle (magenta) positioned hearts. *n* = total number of embryos analyzed. Data shown are pooled from three independent experiments. Statistical comparison was analyzed by one-way ANOVA with Tukey's multiple comparison test; \*\*\**P* < 0.001, \*\*\*\**P* < 0.0001 and ns: *P*  $\geq$  0.05. **(H to K)** Model for calcium-mediated ciliary mechanosensation in the LRO during LR development. At early stages of LR patterning, counterclockwise left-biased flow (curved orange arrow) or ciliary optical bending triggers Pkd2-dependent intraciliary calcium signaling (in cilia, magenta ICOs; in cells, dark blue) on the side of the LRO subjected to ciliary mechanical stimulation (1). Cilia-to-cytosolic LRO calcium (2) is then transmitted to neighboring cells of the mesoderm in a side-biased manner (3), which in turn ultimately direct asymmetric gene expression (4) leading to LR patterning. A, anterior; P, posterior; L, left; R, right.



cilia in the LRO of *pkd2* mutant and knock-down zebrafish embryos, and measured intraciliary calcium levels. Notably, we found a significantly lower incidence of CiliaSPOT-induced intraciliary calcium transients in immotile LRO cilia of both *pkd2* knockdown and *pkd2* knockout embryos (Fig. 3 and movie S10). Further, there was no elevation in cytosolic calcium activity after LRO ciliary bending in *pkd2* mutant embryos (Fig. 3K). This loss of intraciliary calcium transients in optically tweezed *pkd2* mutant embryos confirms that the CiliaSPOT-induced intraciliary calcium transients in WT and *c21orf59* knockdown embryos were not caused by photodamage

or microdamage. These results support a role for Pkd2 as a mechanosensitive calcium channel on cilia in the LRO.

**Ciliary mechanosensation is instructive for LR asymmetry**

Directional LRO fluid flow is essential for asymmetric gene expression of Nodal signaling components during LR development in mice, zebrafish, and *Xenopus* (2, 4, 7-10). We and others previously linked directional fluid flow and ICOs to left-sided degradation of *dand5*, the first asymmetrically expressed gene and an upstream inhibitor of Nodal signaling (7, 46, 47). To test whether ciliary mechanosensing itself

is sufficient for asymmetric *dand5* expression, we utilized optical tweezers to bend cilia in *c21orf59* knockdown zebrafish, which have LR-randomized expression of *dand5* in the LRO (20). Oscillatory deflection of one immotile cilium was performed at the 1 somite stage (1 ss) on the left side of the LRO of *c21orf59* knockdown embryos for 1 hour, within the critical window when initial symmetry breaking occurs in the zebrafish LRO (1-4 ss) (20) (Fig. 4, A to E). After tweezing, embryos were unmounted from the microscope, raised normally until 8-10 ss, and assayed for asymmetric *dand5* expression by in situ hybridization (46, 47). Strikingly, mechanical stimulation of a single

cilium on the left side of the LRO was sufficient to rescue proper right-biased *dand5* expression (Fig. 4F).

Ciliary bending can rescue the laterality of asymmetric organs such as the heart, similar to experiments in the mouse LRO utilizing artificial directional fluid flow (3). We optically bent cilia in *c21orf59* knockdown zebrafish, which normally exhibit complete LR randomization of cardiac jogging, a precursor for asymmetric cardiac looping in zebrafish (illustrated in movie S11) (20, 37). After tweezer stimulation of a single immotile cilium on the left side of the LRO for 1 hour, embryos were raised until 24 hours post fertilization (hpf) and scored for the LR direction of cardiac jogging. Bending a cilium on the left side of the LRO resulted in normal, leftward cardiac jogging (Fig. 4G), similar to the rescue of asymmetric *dand5* expression described above. These rescue data further confirmed that our optical tweezers approach did not negatively affect LR development or embryonic viability. Bending a cilium on the right side of the LRO led to the opposite—rightward cardiac jogging (Fig. 4G). These results indicate that ciliary mechanosensation is sufficient and instructive for both LR asymmetric gene expression and cardiac situs.

Finally, we examined whether *Pkd2* is required for ciliary mechanosensing during cardiac LR patterning by applying the same approach to *pkd2* knockdown embryos, which also have LR randomized cardiac looping and jogging (43, 44). In contrast to *c21orf59* embryos, bending immotile cilia on the left side of the LRO for 1 hour in *pkd2* knockdown embryos failed to rescue proper leftward cardiac jogging (fig. S11), demonstrating the key role of *Pkd2* as a mechanosensor required in LRO cilia for cardiac situs determination. Altogether, our findings establish ciliary force sensing as necessary, sufficient, and instructive for LR asymmetry.

## Discussion

The importance of flow in the LRO has long been realized and a variety of experimental investigations have shown that its absence leads to aberrant LR asymmetry of molecular markers and organ development (14, 15, 17). A large body of data has accumulated that are consistent with flow mediating these LR differences by the transport of morphogens or by mechanosensation, but without clear demonstration of either. Our results directly show that LRO ciliary mechanosensation is both necessary and sufficient for molecular and morphological LR asymmetry.

Using carefully controlled optomechanical manipulations of cilia within the LRO, we provide evidence that *Pkd2*-dependent intraciliary calcium transients are mechanically generated in the LRO and that LRO ciliary mechanosensation is determinative for LR development

(Fig. 4, H to K). By applying an oscillatory bending force directly to cilia for up to an hour, we emulated physiological conditions for *in vivo* cilia deflection at the LRO and demonstrated that oscillatory bending on a scale of seconds to minutes is critical to stimulate a calcium response in LRO cilia. This similarity to endogenous LRO ICOs (20, 36), that occur at a low frequency (ranging from 3.3 to 5.2 min) (20), indicates that a single cilium requires repetitive and consistent mechanical stimulation before a calcium signal is transmitted to the cell. This allows the cilium to discriminate between true (repetitive) and false (random) stimuli by filtering out extraneous biological noise in tissues subjected to abundant biomechanical forces, including directional extracellular fluid flow and nondirectional cytoskeletal movements. We posit that the cilium's noise filtering capability may be adaptable, as the filter threshold in WT embryos with intrinsic flow appears to be higher than in flowless embryos as suggested by the lower number of responses in WT LRO cilia (Fig. 3, I and J) compared with *c21orf59* cilia (Fig. 3, C and D).

Our results suggest that LRO cilia may be heterogeneous, as among all the LRO cilia we optically tweezed, 20 to 30% responded positively to the oscillatory optical bending (Fig. 3, C and I). Notably, our previous study found the same percentage of cilia that display ICOs in WT LROs with endogenous flow (20). These observations, coupled with another report that found a similar percentage of immotile cilia in the LRO (31), suggest that a distinct subpopulation of LRO cilia function as mechanosensors as hypothesized in the two-cilia model of LR development (1, 19). Although our findings experimentally validate this model, we cannot definitively rule out that a morphogen participates in LR development (2, 18). It remains possible that mechanosensation and chemosensation cooperate at the LRO; for example, mechanical cues might expose ligand receptor sites on cilia or *Pkd2* itself.

Investigating endogenous ciliary dynamics in WT LROs revealed that left-sided LRO cilia experienced a greater angle displacement than right-sided ones (fig. S2B). We found that the 75th percentile of WT cilia on the left side of the LRO exhibited an angular displacement of  $31.2 \pm 1.5^\circ$  (mean  $\pm$  SEM, fig. S2F), which mirrored the mean angular displacement of tweezed cilia that responded positively to optical bending ( $31.7 \pm 2.5^\circ$ ; Fig. 2E). These results suggest that a greater displacement angle due to force exerted by directional flow increases the likelihood of an intraciliary calcium transient on the left-side of the LRO.

Our conclusions in the zebrafish LRO utilizing CiliaSPOT mirrored results in the mouse LRO in an accompanying research article (48). Both studies independently interrogated the

function of cilia as calcium-mediated mechanosensors in the LRO using different experimental models and cilia deflection approaches. Despite this, we found surprising similarities in ciliary mechanosensation and intraciliary calcium transients between the mouse and zebrafish LRO, emphasizing an evolutionarily conserved mechanism for cilia mechanotransduction during LR development in vertebrates with ciliated LROs. Intriguing findings from previous work in mice and zebrafish point to slow, localized LRO flow currents as sufficient for normal LR patterning (9, 49), suggesting that fast, coordinated LRO flow at later stages is not essential for initiating asymmetry. Our work demonstrates that mechanical stimulation of a single cilium in the LRO for extended periods of time was determinative for molecular and cardiac asymmetry, resolving prior discrepancies (24). These findings show that ciliary mechanosensing is a fundamental and potent cellular signaling mechanism in development and disease, as a single ciliated cell was sufficient to create chiral vertebrate asymmetry. Finally, our study reveals that, in addition to biochemical and molecular mechanisms, small physical forces at the level of single cells and organelles play essential roles in shaping the bilateral body of the developing embryo.

## REFERENCES AND NOTES

1. J. McGrath, S. Somlo, S. Makova, X. Tian, M. Brueckner, *Cell* **114**, 61–73 (2003).
2. Y. Okada *et al.*, *Mol. Cell* **4**, 459–468 (1999).
3. S. Nonaka, H. Shiratori, Y. Saijoh, H. Hamada, *Nature* **418**, 96–99 (2002).
4. S. Nonaka *et al.*, *Cell* **95**, 829–837 (1998).
5. S. Yoshida *et al.*, *Science* **338**, 226–231 (2012).
6. M. Levin, R. L. Johnson, C. D. Stern, M. Kuehn, C. Tabin, *Cell* **82**, 803–814 (1995).
7. A. Schweickert *et al.*, *Curr. Biol.* **20**, 738–743 (2010).
8. J. J. Essner, J. D. Amack, M. K. Nyholm, E. B. Harris, H. J. Yost, *Development* **132**, 1247–1260 (2005).
9. P. Sampaio *et al.*, *Dev. Cell* **29**, 716–728 (2014).
10. N. Okabe, B. Xu, R. D. Burdine, *Dev. Dyn.* **237**, 3602–3612 (2008).
11. J. J. Essner *et al.*, *Nature* **418**, 37–38 (2002).
12. A. G. Kramer-Zucker *et al.*, *Development* **132**, 1907–1921 (2005).
13. W. Supatto, S. E. Fraser, J. Vermot, *Biophys. J.* **95**, L29–L31 (2008).
14. L. Djenoune, K. Berg, M. Brueckner, S. Yuan, *Nat. Rev. Cardiol.* **19**, 211–227 (2022).
15. R. B. Little, D. P. Norris, *Semin. Cell Dev. Biol.* **110**, 11–18 (2021).
16. R. R. Ferreira, A. Vilfan, F. Jülicher, W. Supatto, J. Vermot, *eLife* **6**, e25078 (2017).
17. R. R. Ferreira, H. Fukui, R. Chow, A. Vilfan, J. Vermot, *J. Cell Sci.* **132**, jcs213496 (2019).
18. Y. Tanaka, Y. Okada, N. Hirokawa, *Nature* **435**, 172–177 (2005).
19. C. J. Tabin, K. J. Vogan, *Genes Dev.* **17**, 1–6 (2003).
20. S. Yuan, L. Zhao, M. Brueckner, Z. Sun, *Curr. Biol.* **25**, 556–567 (2015).
21. D. Takao *et al.*, *Dev. Biol.* **376**, 23–30 (2013).
22. H. A. Praetorius, K. R. Spring, *J. Membr. Biol.* **184**, 71–79 (2001).
23. S. M. Nauili *et al.*, *Nat. Genet.* **33**, 129–137 (2003).
24. M. Delling *et al.*, *Nature* **531**, 656–660 (2016).
25. S. Su *et al.*, *Nat. Methods* **10**, 1105–1107 (2013).
26. A. Ashkin, K. Schütze, J. M. Dziedzic, U. Euteneuer, M. Schliwa, *Nature* **348**, 346–348 (1990).
27. A. Ashkin, J. M. Dziedzic, J. E. Bjorkholm, S. Chu, *Opt. Lett.* **11**, 288 (1986).
28. K. Svoboda, S. M. Block, *Annu. Rev. Biophys. Biomol. Struct.* **23**, 247–285 (1994).
29. A. K. O'Connor *et al.*, *Cilia* **2**, 8 (2013).
30. J. G. Goetz *et al.*, *Cell Rep.* **6**, 799–808 (2014).
31. B. Tavares *et al.*, *eLife* **6**, e25165 (2017).
32. J. Huisken, D. Y. Stainier, *Opt. Lett.* **32**, 2608–2610 (2007).
33. T. V. Truong, W. Supatto, D. S. Koos, J. M. Choi, S. E. Fraser, *Nat. Methods* **8**, 757–760 (2011).

34. C. Battle, C. M. Ott, D. T. Burnette, J. Lippincott-Schwartz, C. F. Schmidt, *Proc. Natl. Acad. Sci. U.S.A.* **112**, 1410–1415 (2015).
35. A. Resnick, *J. Biomed. Opt.* **15**, 015005 (2010).
36. K. Mizuno *et al.*, *Sci. Adv.* **6**, eaba1195 (2020).
37. C. Austin-Tse *et al.*, *Am. J. Hum. Genet.* **93**, 672–686 (2013).
38. M. T. Boskovski *et al.*, *Nature* **504**, 456–459 (2013).
39. D. Moreau, C. Lefort, R. Burke, P. Leveque, R. P. O'Connor, *Biomed. Opt. Express* **6**, 4105–4117 (2015).
40. P. G. DeCaen, M. Delling, T. N. Vien, D. E. Clapham, *Nature* **504**, 315–318 (2013).
41. M. Delling, P. G. DeCaen, J. F. Doerner, S. Febvay, D. E. Clapham, *Nature* **504**, 311–314 (2013).
42. S. J. Kleene, N. K. Kleene, *Am. J. Physiol. Renal Physiol.* **320**, F1165–F1173 (2021).
43. P. Pennekamp *et al.*, *Curr. Biol.* **12**, 938–943 (2002).
44. B. W. Biggrove, B. S. Snarr, A. Emrazian, H. J. Yost, *Dev. Biol.* **287**, 274–288 (2005).
45. J. Schottenfeld, J. Sullivan-Brown, R. D. Burdine, *Development* **134**, 1605–1615 (2007).
46. S. S. Lopes *et al.*, *Development* **137**, 3625–3632 (2010).
47. H. Hashimoto *et al.*, *Development* **131**, 1741–1753 (2004).
48. T. A. Katoh *et al.*, *Science* **379**, 66–71 (2023).
49. K. Shinohara *et al.*, *Nat. Commun.* **3**, 622 (2012).
50. L. Djenoune *et al.*, CiliaNet: a deep learning tool for cilia analysis, v10, Zenodo (2022); <https://doi.org/10.5281/zenodo.7417672>

## ACKNOWLEDGMENTS

We thank M. Khokha for insightful discussions; H. Shroff, J. Huiskens, R. Power, J. Choi, and M. Guo for providing light sheet microscopy advice; D. Sosnovik for helpful suggestions regarding optical thermometer experiments; Z. Sun, L. Trinh, and Y. Li for advice on zebrafish experiments and sharing lines; S. Somlo, Y. Cai, and S. Makova for sharing cell lines; M. Khokha, S. Makova, and Z. Sun for critical feedback on the manuscript; and A. Brugger, N. Djenoune, and M. Jones for technical assistance. **Funding:** This work was supported by the American Heart Association (Career Development Award 940516 to S.Y., Postdoctoral Fellowship Award 830304 to L.D., Transformational Project Award 969048 to S.Y.), the Charles Hood Foundation (Child Health Award to S.Y.), the Gordon and Betty Moore Foundation (grant 3396 to S.E.F.), the Hassenfeld Foundation (Scholar Award to S.Y.), Massachusetts General Hospital (Institutional funds from Department of Medicine and Cardiology Division to S.Y.), the National Institutes of Health (Outstanding Investigator Award 1R35HL145249 to M.B., Pathway to Independence Award 1K99HD086274 to S.Y., grant 1R01HL151704 to C.T.N., grant 1R01HL165241 to S.Y.), the National Science Foundation (grant 1608744 to S.E.F.), University of Southern California Translational Imaging Center (S.E.F. and T.V.T.), and Yale University (Institutional funds from Departments of Biochemistry and Biophysics to J.H., and Department of Pediatrics to S.Y.). **Author contributions:** Conceptualization: L.D., M.M., M.B., and S.Y. Methodology: L.D., M.M., T.V.T., C.T.N., S.E.F., J.H., and S.Y. Investigation: L.D., M.M., and S.Y. Funding acquisition: L.D., C.T.N., S.E.F., M.B., J.H., and S.Y. Project administration: S.E.F., M.B., J.H., and S.Y. Supervision: S.E.F., M.B., J.H., and S.Y. Writing – original draft: L.D., M.M., and S.Y. Writing – review and editing: all authors. **Competing interests:** Authors declare that they have no competing interests. **Data and materials availability:** All data are available in the manuscript or supplementary materials. Zebrafish lines and plasmids are available upon request. CiliaNet is available on GitHub at <https://github.com/shiaulouyuan/CiliaNet> and archived on Zenodo (50). **License information:** Copyright © 2023 the authors, some rights reserved; exclusive licensee American Association for the Advancement of Science. No claim to original US government works. <https://www.sciencemag.org/about/science-licenses-journal-article-reuse>

## SUPPLEMENTARY MATERIALS

science.org/doi/10.1126/science.abq7317  
Materials and Methods  
Figs. S1 to S11  
Tables S1 and S2  
References (51–73)  
MDAR Reproducibility Checklist  
Movies S1 to S11

View/request a protocol for this paper from *Bio-protocol*.

Submitted 9 May 2022; resubmitted 3 November 2022  
Accepted 9 December 2022  
10.1126/science.abq7317

## GLACIERS

## Global glacier change in the 21st century: Every increase in temperature matters

David R. Rounce<sup>1,2\*</sup>, Regine Hock<sup>2,3</sup>, Fabien Maussion<sup>4</sup>, Romain Hugonnet<sup>5,6,7</sup>, William Kochtitzky<sup>8,9</sup>, Matthias Huss<sup>5,6,10</sup>, Etienne Berthier<sup>7</sup>, Douglas Brinkerhoff<sup>11</sup>, Loris Compagno<sup>5,6</sup>, Luke Copland<sup>8</sup>, Daniel Farinotti<sup>5,6</sup>, Brian Menounos<sup>12,13</sup>, Robert W. McNabb<sup>14</sup>

Glacier mass loss affects sea level rise, water resources, and natural hazards. We present global glacier projections, excluding the ice sheets, for shared socioeconomic pathways calibrated with data for every glacier. Glaciers are projected to lose  $26 \pm 6\%$  ( $+1.5^\circ\text{C}$ ) to  $41 \pm 11\%$  ( $+4^\circ\text{C}$ ) of their mass by 2100, relative to 2015, for global temperature change scenarios. This corresponds to  $90 \pm 26$  to  $154 \pm 44$  millimeters sea level equivalent and will cause  $49 \pm 9$  to  $83 \pm 7\%$  of glaciers to disappear. Mass loss is linearly related to temperature increase and thus reductions in temperature increase reduce mass loss. Based on climate pledges from the Conference of the Parties (COP26), global mean temperature is projected to increase by  $+2.7^\circ\text{C}$ , which would lead to a sea level contribution of  $115 \pm 40$  millimeters and cause widespread deglaciation in most mid-latitude regions by 2100.

Glaciers, here referring to all glacial land ice excluding the Greenland and Antarctic ice sheets, are responsible for  $21 \pm 3\%$  of sea level rise from 2000 to 2019, contributing  $0.74 \pm 0.04$  mm sea level equivalent (SLE)  $\text{yr}^{-1}$  (1). Projections suggest this contribution could increase to 2.5 mm SLE  $\text{yr}^{-1}$  by 2100 (2). Glaciers are also a critical water resource for ~1.9 billion people (3), and projected losses will alter water availability impacting annual and seasonal runoff (4). Glacier-related hazards, including glacier outburst floods, are also expected to change in frequency and magnitude over the next century as a result of mass loss (5). Projecting the magnitude, spatial pattern, and timing of glacier mass loss is therefore essential to support climate adaptation and mitigation efforts for communities ranging from the coast to the high mountains.

Previous projections of glacier mass loss from the glacier model intercomparison project (GlacierMIP) (2) estimated glacier contribution to sea level rise for ensembles of representative concentration pathways (RCPs), and

results were extended to shared socioeconomic pathways (SSPs) using statistical models of these simulations (6). GlacierMIP provided these projections at regional scales based on simulations from 11 glacier evolution models that varied with respect to the complexity of model physics, simulated physical processes, model calibration, spatial resolution, and modeling domain. Calibration data varied from in situ measurements of less than 300 of the world's more than 215,000 glaciers to regional geodetic and/or gravimetric mass balance observations. Furthermore, only one global model simulated glacier dynamics using a flowline model (7), whereas all others relied on empirical volume-area scaling or parameterizations of mass redistribution; only one model accounted for frontal ablation (i.e., the sum of iceberg calving and submarine melt) of marine-terminating glaciers (8), whereas all others treated any glacier as land-terminating; further, no global model accounted for debris cover. Existing multimodel projections (2, 6, 9) are thus limited to regional scales and neglect key physical processes controlling glacier mass loss.

We produce a set of global glacier projections for every glacier on Earth for SSPs from 2015 to 2100 by leveraging global glacier mass balance data (1) and near-global frontal ablation data (10–13). To provide policy-relevant scenarios, our projections are grouped based on mean global temperature increases by the end of the 21st century compared with pre-industrial levels to explicitly link differences in glacier mass loss, sea level rise, and the number of glaciers that vanish in response to changes in mean global temperature. Our glacier evolution model, a hybrid of the Python Glacier Evolution Model (PyGEM) (14, 15) and Open Global Glacier Model (OGGM) (7), enables us to produce global glacier projections that explicitly account for glacier dynamics using a

<sup>1</sup>Department of Civil and Environmental Engineering, Carnegie Mellon University, Pittsburgh, PA, USA. <sup>2</sup>Geophysical Institute, University of Alaska Fairbanks, Fairbanks, AK, USA. <sup>3</sup>Department of Geosciences, University of Oslo, Oslo, Norway. <sup>4</sup>Department of Atmospheric and Cryospheric Sciences, University of Innsbruck, Innsbruck, Austria. <sup>5</sup>Laboratory of Hydraulics, Hydrology and Glaciology (VAW), ETH Zürich, Zurich, Switzerland. <sup>6</sup>Swiss Federal Institute for Forest, Snow and Landscape Research (WSL), Birmensdorf, Switzerland. <sup>7</sup>LEGOS, Université de Toulouse, CNES, CNRS, IRD, UPS, Toulouse, France. <sup>8</sup>Department of Geography, Environment and Geomatics, University of Ottawa, Ottawa, Ontario, Canada. <sup>9</sup>School of Marine and Environmental Programs, University of New England, Biddeford, ME, USA. <sup>10</sup>Department of Geosciences, University of Fribourg, Fribourg, Switzerland. <sup>11</sup>Department of Computer Science, University of Montana, Missoula, MT, USA. <sup>12</sup>Geography Earth and Environmental Sciences, University of Northern British Columbia, Prince George, BC, Canada. <sup>13</sup>Hakai Institute, Campbell River, BC, Canada. <sup>14</sup>School of Geography and Environmental Sciences, Ulster University, Coleraine, UK.  
\*Corresponding author. Email: [drounce@cmu.edu](mailto:drounce@cmu.edu)